JMEPEG
https://doi.org/10.1007/s11665-025-11091-y

1059-9495/$19.00

ORIGINAL RESEARCH ARTICLE

Analysis of Hot Forging of a Bainitic Steel Hardened by Continuous Cooling Using Wedge Test

André Rosiak, Luana De Lucca de Costa, Thomas Gomes dos Santos, and Lirio Schaeffer

Submitted: 10 September 2024 / Revised: 9 February 2025 / Accepted: 21 February 2025

This article investigates the forgeability of a microalloyed steel 0.18C-1.38Mn-0.36Si-0.47Cr-0.03Mo-0.05Al-0.04Nb-0.01Ti, with emphasis on its application in the hot forging process followed by continuous cooling, aiming to eliminate traditional quenching and tempering heat treatments. The research seeks to understand how thermomechanical parameters influence the microstructure and material behavior during processing. The approach included experiments and numerical simulations, as well as detailed analysis of the prior austenitic structure. The wedge test was employed to correlate microstructural changes with deformation under different temperatures. The results show that controlled deformation, combined with high forging temperatures, promotes recrystallization and grain refinement, resulting in a uniform bainitic microstructure and high hardness levels. The steel showed potential for application in small-volume parts, offering a cost-effective and energy-efficient solution by eliminating the need for heat treatments.

Keywords bainitic steel, continuous cooling, hot forging, wedge test

1. Introduction

The global forged products market was valued at USD 81.13 billion in 2023 and is projected to grow from USD 87.06 billion in 2024 to USD 157.94 billion by 2032, showing a compound annual growth rate of 7.6% during the forecast period (Ref 1). Among the global megatrends, the fight against climate change is one of the key drivers of this market. The increasing pressure to reduce CO_2 emissions, combined with increasingly stringent government regulations, has led forging companies to innovate and develop more sustainable processes.

One of these innovations is the forging of steels that eliminate traditional heat treatments (Ref 2, 3). High-performance forgings are typically produced from quench and tempered (Q&T) steels, which achieve a balance of properties through a three-step heat treatment: austenitizing, quenching, and tempering, transforming brittle martensite into a technically suitable tempered material. In recent decades, precipitation-hardened ferritic-pearlitic (PHFP) steels have been developed to simplify the heat treatment route (Ref 4). These steels achieve their final properties through controlled cooling directly from the forging heat, resulting in significant reductions in process costs, energy demand, and consequently, emissions (Ref 5).

More recently, steels with more complex microstructures and chemical compositions have been developed, allowing for superior properties (Ref 6). Air-cooled bainitic (Ref 7-11), bainitic-martensitic (Ref 12), and martensitic steels (Ref 13-15) have already shown potential to replace Q&T steels in various applications, emerging as viable alternatives to meet the market's sustainability and efficiency demands.

Designing the forging process for continuously cooled steels from forging requires the careful selection of conditions that ensure the desired microstructure and mechanical properties. This can only be achieved through a deep understanding of the complex interactions between metallurgical phenomena and the thermomechanical parameters of the process. An efficient technique for evaluating these interactions is the wedge test (Ref 16-20). In this study, a comprehensive analysis of the forgeability of a steel with the composition 0.18C-1.38Mn-0.36Si-0.47Cr-0.03Mo-0.05Al-0.04Nb-0.01Ti is conducted using this technique. The research combines simulations and experiments to investigate the relationship between microstructural changes and the material's deformation behavior. Through this integrated approach, the study seeks to understand how process variables influence the final performance of the steel, providing valuable insights for developing more efficient and precise forging processes.

2. Materials and Methods

The material investigated in this study is a low-carbon steel microalloyed with Ti and Nb, with the composition 0.18C-1.38Mn-0.36Si-0.47Cr-0.03Mo-0.05Al-0.04Nb-0.01Ti. The additions of manganese, chromium, and molybdenum are intended to enhance hardenability. In the initial condition, the material exhibits a microstructure typical of a slowly cooled low-carbon steel, consisting of ferrite and dispersed islands of pearlite.

The reduction in production costs is a crucial factor in the selection of steel for forging. In this sense, the application of cost-optimized alloy concepts becomes essential. The steel

André Rosiak, Luana De Lucca de Costa, Thomas Gomes dos Santos, and **Lirio Schaeffer**, Metal Forming Innovation Center (CBCM), Federal University of Rio Grande do Sul, Porto Alegre, Brazil. Contact e-mail: andre.rosiak@ufrgs.br.

Published online: 31 March 2025

investigated in this work presents lower levels of volatile and high-cost alloying elements, such as molybdenum and nickel, compared to other modern advanced steels for forging. Furthermore, the chromium content is also reduced, which contributes to making raw material costs more rational, increasing the competitiveness of the proposal. Additionally, the lower alloy content provides environmental advantages, especially in the case of molybdenum, whose significant impact on energy demand and material footprint makes it a particularly critical element (Ref 2).

2.1 Evaluation of Austenitization Parameters

The final properties of forgings subjected to continuous cooling are highly sensitive to the austenitization conditions of the material. For this reason, the analysis of the material's forgeability begins with the evaluation of the effect of the austenitization parameters on the prior austenitic structure.

The effects of time (t_γ) and temperature (T_γ) of austenitization on the prior austenitic grain size were analyzed through different austenitization treatments, as detailed in Table 1.

In the heat treatments, cubic samples with 20-mm edges were used. Type K thermocouples were inserted with the hot junction positioned at the core of the geometries for temperature monitoring. After austenitization in a chamber-type resistive furnace, all the specimens were water-quenched. The prior austenitic structure was analyzed by optical microscopy after chemical etching with picral reagent.

The quantitative analysis of the prior austenitic structure was performed using the circular intercept method, as specified by the American Society for Testing and Materials (Ref 21). This technique, recommended for materials with non-equiaxed grain structures, allows for the determination of austenitic grain size. For each condition analyzed, at least 1000 grains were measured.

The heating time of 0 min ($t_\gamma = 0$) corresponds to the moment when the furnace's austenitization temperature reaches the core of the specimen. The times of 10, 20, and 40 min are counted from $t_\gamma = 0$.

Table 1 Heat treatments performed to analyze the effect of austenitization parameters on the material's prior structure

Temperature, T_γ, °C	Time, t_γ, min
1000	0
	10
	20
	40
1100	0
	10
	20
	40
1200	0
	10
	20
	40

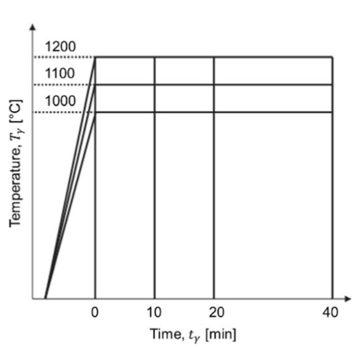

2.2 Wedge Test

To comprehensively evaluate the effect of thermomechanical processing on the material, wedge tests were conducted. These tests aim to establish the correlation between deformation, microstructural changes, and hot forgeability at different temperatures.

In the wedge test, a wedge-shaped specimen is forged between parallel flat dies. As shown in Fig. 1, the samples consist of a portion with a constant height and a region with variable height, while maintaining a fixed width. The constant speed of the upper die, combined with the variation in the sample height and friction, generates a heterogeneous distribution of strain and strain rate along the length and across any section. Through numerical analysis of the test, it is possible to predict local strains and strain rates and establish correlations with microstructural changes and hot forgeability as a function of temperature.

In each experiment, the specimen is heated in a resistive furnace until its core reaches the desired temperature ($t_\gamma = 0$). This time was 13, 9, and 7 min for temperatures of 1000 °C, 1100 °C, and 1200 °C, respectively. It is then quickly transferred to the press for the hot forming stage. The wedges were subjected to a 23-mm reduction in height by the action of flat dies preheated to 180 °C and coated with graphite-based lubricant. The tests were carried out on an FKL hydraulic press with a speed of 6.5 mm/s and a capacity of 700 tons. After forging, the wedges were air-cooled to room temperature.

The tests were performed at three heating temperatures (T_0): 1000, 1100, and 1200 °C. Type K thermocouples were inserted with the hot junction positioned at the core of the wedges for temperature monitoring.

During the tests, force and displacement data were collected. The displacement of the press was monitored by a linear variable differential transformer (LVDT), and the force was measured by a load cell mounted on the lower table of the press. The signals were acquired using a Spider 8 device from HBM and processed with Catman Express software.

The forged wedges were sectioned, and the microhardness profile of the longitudinal section was constructed. The microstructure was analyzed using optical microscopy and scanning electron microscopy (SEM). Conventional metallographic preparation techniques were applied to the longitudinal section of the forged wedges. The chemical reagent used for revealing the microstructure was 2% Nital.

To analyze the prior grain size of the forged wedges, some of the specimens were water-quenched after forming. The prior austenitic structure was analyzed by optical microscopy after chemical etching with picral reagent (a solution composed of 100 mL of distilled water, 10 g of picric acid, and 2 mL of hydrochloric acid.).

2.3 Inverse Analysis Using Finite Elements

The inverse analysis of the experimental procedure was carried out using the Qform UK software. Utilizing the finite element method (FEM), 3D simulations of the tests were performed. The simulations were divided into the following stages:

(i) Transfer of the wedge from the furnace to the press: This stage lasts for 8 seconds and calculates the thermal losses of the piece to the environment.

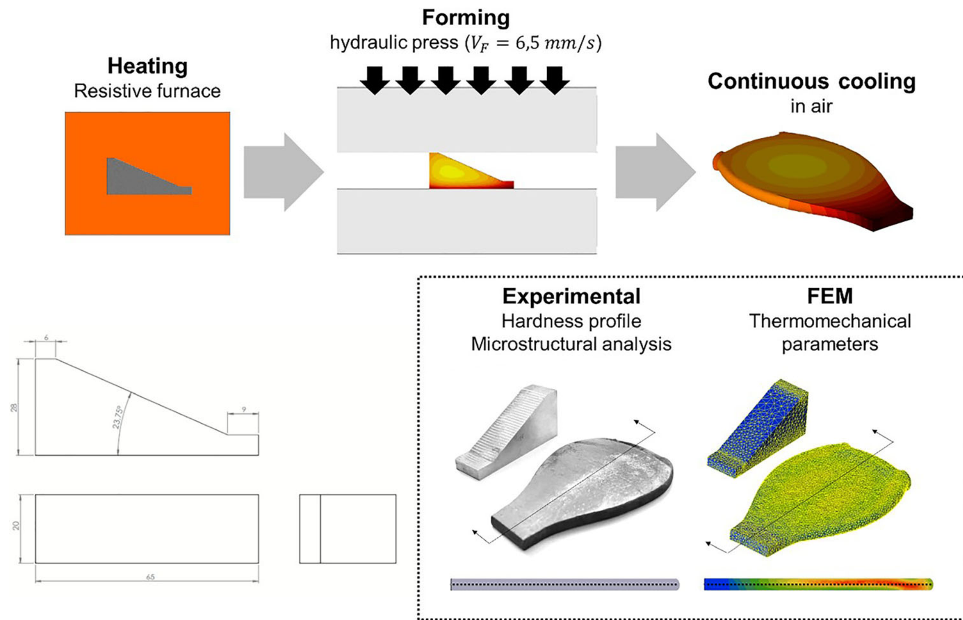

Fig. 1 Wedge test

(ii) Positioning of the wedge on the lower die: This stage lasts for 2 seconds and calculates the thermal losses of the piece to the environment and to the lower die.
(iii) Forging.
(iv) Extraction of the wedge: This stage lasts for 3 seconds and calculates the thermal losses of the piece to the environment and to the lower die.
(v) Continuous cooling: This stage calculates the thermal losses of the piece to the environment.

The duration of each stage was defined by the average values observed during the experimental procedure. The experimental data on force, displacement, and temperature were used to calibrate the numerical models. Table 2 lists the information related to the numerical models.

The information related to the work material was entered into the software library. The Hensel-Spittel equation (Eq 1) was used to characterize the mechanical behavior of the material during hot forming. Table 3 lists the parameters of the Hensel-Spittel equation for the alloy investigated.

$$k_f = A \cdot e^{m_1 \cdot \vartheta} \cdot \varphi^{m_2} \cdot \dot{\varphi}^{m_3} \cdot e^{\frac{m_4}{\varphi}} \cdot (1+\varphi)^{m_5 \cdot \vartheta} \cdot e^{m_7 \cdot \varphi} \cdot \dot{\varphi}^{m_8 \cdot \vartheta} \cdot \vartheta^{m_9} \qquad \text{(Eq 1)}$$

where A and m_1 to m_9 are material constants that must be determined experimentally.

Table 2 Input data for the numerical models

Mesh type	Adaptive triangular
Workpiece temperature	Experimentally calibrated
Tool material	AISI H13 (Rigid)
Tool temperature	180, °C
Tool speed	6.5, mm/s
Friction coefficient	0.4 (Levanov)

3. Results and Discussions

3.1 Evaluation of Austenitization Parameters

Figure 2 presents representative examples of the microstructural examination of prior austenite after austenitization at different temperatures and holding times. Figure 3 illustrates the variation in the average austenite grain size as a function of austenitization temperature and time, while Table 4 summarizes the quantitative results regarding the influence of processing parameters on the prior austenite grain size. As expected, the austenite grain size increases with the rise in soaking temperature.

The growth of austenite grains occurs primarily due to the migration of grain boundaries, a thermally activated process in which the mobility of these boundaries intensifies with increasing temperature (Ref 22). Additionally, the rise in austenitization temperature and time affects the size of precipitates and the volume fraction of these particles. These factors play a key role in restricting the movement of grain boundaries and, consequently, in the kinetics of grain growth. As the austenitization temperature and time increase, the volume fraction of the particles decreases and their size increases. This change in the precipitate distribution reduces their effectiveness in pinning the grain boundaries, thereby facilitating the growth of austenite grains (Ref 23).

The sensitivity of grain size to austenitization time varies according to the temperature analyzed. During austenitization at 1000 °C, the grain size remains nearly constant, around 16 μm, for soaking times of up to 10 min. However, measurements taken after 20 and 40 min indicate an almost linear increase in grain size, reaching 23 μm after 40 min of soaking.

When the temperature is raised to 1100 °C, a nearly linear increase in grain size is observed between 0 and 20 min of soaking, from 35 to 40 μm. After 20 min, the grain growth rate changes, and the grain size reaches 43 μm after 40 min.

Table 3 Parameters of the Hensel-Spittel equation for the investigated alloy

A, MPa	m_1	m_2	m_3	m_4	m_5	m_7	m_8	m_9
1510	− 0.004	0.24	− 0.03	− 0.002	− 0.0006	− 0.13	0.0002	0.28

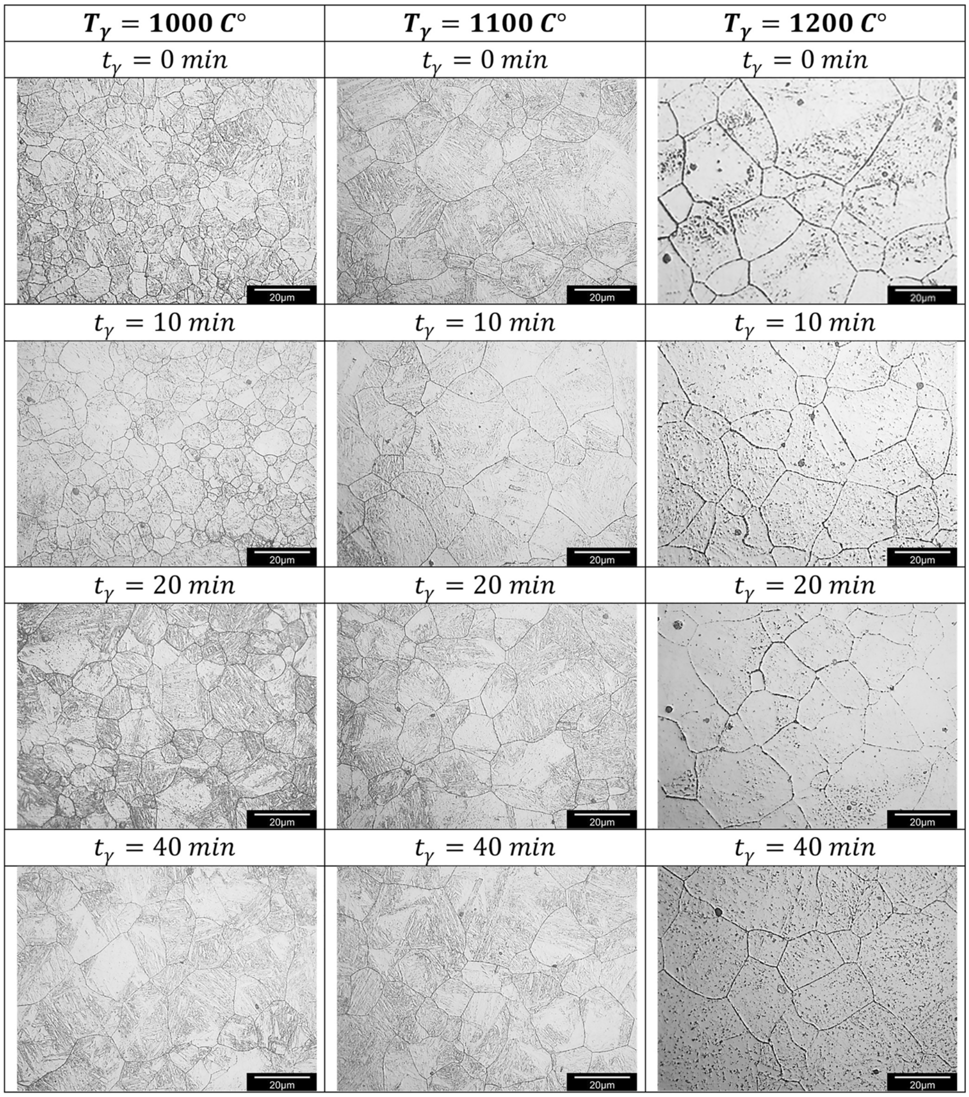

Fig. 2 Optical micrographs of prior austenite after different austenitization temperatures and times

At 1200 °C, the grain growth follows a nearly linear behavior up to 20 min of soaking, with the grain size increasing from 47 to 58 μm. Similar to the observation at 1100 °C, after 20 min, the grain growth rate decreases, and the grain size reaches 62 μm after 40 min.

The values presented in Fig. 3 are consistent with those reported by Erisir et al. (Ref 24), who studied a steel with similar contents of C, Ti, Nb, and N. The control of grain growth in microalloyed steels during thermomechanical processing depends crucially on second-phase particles. The addition of Ti and Nb microalloys results in the formation of nitride, carbide, and carbonitride dispersions, which are effective in minimizing the growth of austenite grains. With the aid of energy-dispersive x-ray spectroscopy, Ti and Nb precipitates smaller than 1 μm were identified in the austenitized samples. Due to their small size, these particles are not visible in Fig. 2, which shows larger particles corresponding to non-metallic inclusions.

Not all Ti and Nb precipitates remain stable at processing temperatures. Consequently, alloys containing Nb and Ti may be susceptible to abnormal austenite grain growth (Ref 25, 26). The emergence of abnormally large grains compromises the homogeneity of the prior microstructure. This phenomenon can be assessed using the variability parameter (ΔPAG), which corresponds to the ratio between the standard deviation and the average grain size (Ref 27). It was observed that for $\Delta PAG \geq 0.3$, abnormal grain growth occurs. This behavior was identified during austenitization processes conducted at

1100 °C and 1200 °C, with treatment times of 20 and 40 min. Figure 4 illustrates this abrupt growth, resulting in grains with an average diameter exceeding 100 μm. The rapid abnormal growth of austenite grains is attributed to the dissolution of carbides. The localized absence of effective precipitates to stabilize grain boundaries creates favorable conditions for accelerated or abnormal grain growth. This is undesirable as it compromises the final microstructure refinement, negatively impacting mechanical properties such as toughness and ductility (Ref 28).

3.2 Wedge Test

To ensure greater representativeness of the results, the wedge tests were repeated five times for each condition analyzed. Macro- and microscopic analyses confirmed that the forged parts did not exhibit any specific cracks or surface damage.

Figure 5 shows the thermal histories of the forged wedges starting from the heating temperatures (T_0) of 1000, 1100, and 1200 °C. The solid lines represent the experimental data, while the dotted lines represent the results obtained from finite element models.

The temperature evolution over time shows a similar behavior for the three analyzed temperatures. Initially, there is a slight drop in temperature due to the transfer of the piece from the furnace to the press and the positioning of the wedge in the lower die, causing the actual forging temperature to differ from T_0. Subsequently, an abrupt temperature drop occurs with the start of forging. The low speed of the forming equipment causes significant cooling of the piece, which reaches temperatures between 400 °C and 500 °C after forming. Upon completion of forging and the beginning of continuous cooling, the temperature shows a slight increase, followed by a gradual drop until reaching room temperature.

Figure 6 also shows the evolution of force as a function of press displacement for the three conditions analyzed. The solid lines represent the experimental data, while the dotted lines represent the results obtained from the finite element models. As expected, the force required to deform the wedge increases as the forging temperature decreases.

The comparison between the experimental force–displacement curves and the numerical results is an effective method for validating finite element simulations. It is observed that the numerical results show excellent agreement with the experimental data, which is also confirmed by the thermal history records. This demonstrates that the boundary conditions of the models, such as friction, die cooling, and heat transfer to the

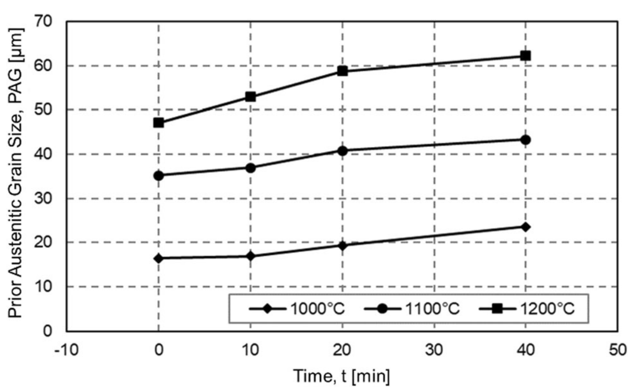

Fig. 3 Variation of the average prior austenitic grain size as a function of austenitization temperature and time

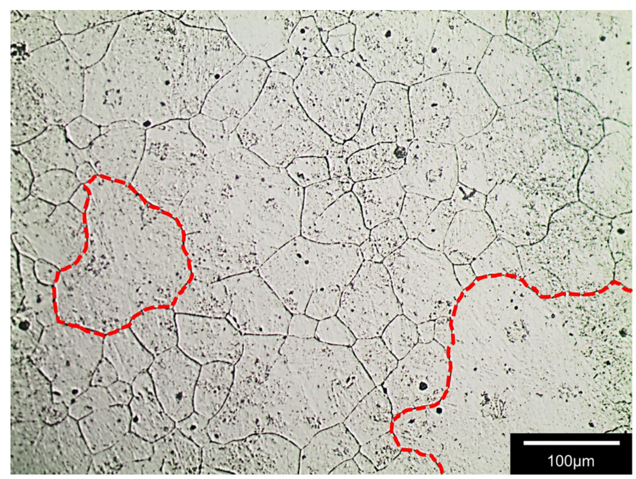

Fig. 4 Abnormal growth of austenite grains ($T_\gamma = 1200^\circ$C; $t_\gamma = 20$min)

Table 4 Effect of processing parameters on prior austenite grain size

Temperature, T_γ, °C	Time, t_γ, min	Prior austenite grain size, PAG, μm	Standard deviation, μm	ASTM grain size, G	Variability parameter, ΔPAG
1000	0	16.4	2.6	2.6	0.16
	10	16.9	2.9	2.9	0.17
	20	19.4	2.3	2.3	0.12
	40	23.6	3.9	3.9	0.17
1100	0	35.1	10.5	7.9	0.23
	10	37.0	11.4	8.9	0.24
	20	40.8	12.3	12.3	0.30
	40	43.3	11.9	13.1	0.30
1200	0	47.1	14.7	10.1	0.21
	10	52.9	15.3	12.2	0.23
	20	58.7	16.4	18.2	0.31
	40	62.2	16.9	18.7	0.30

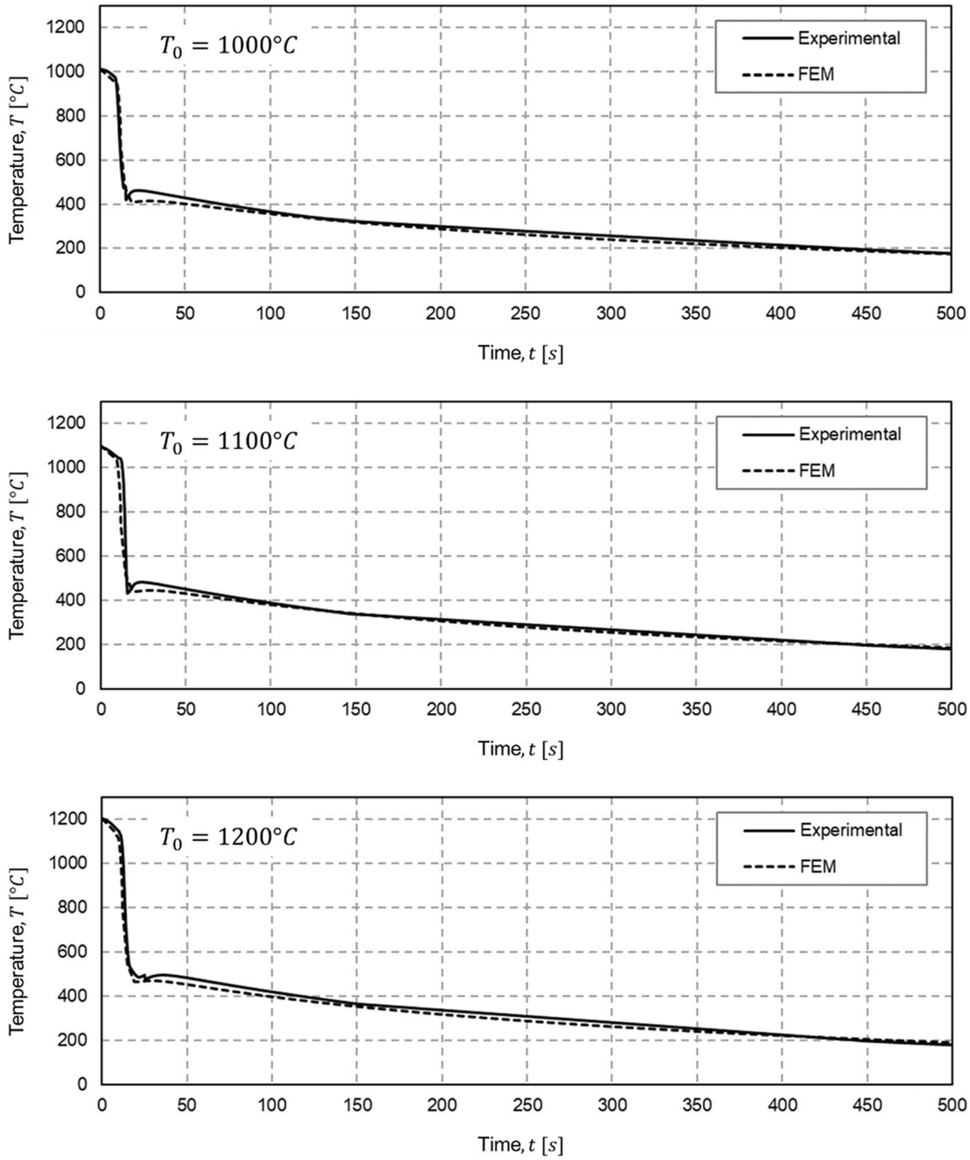

Fig. 5 Thermal histories of the forged wedges

environment, were simulated accurately to reflect the real process conditions. Thus, it is possible to achieve a strong similarity between the loading behavior and the microstructural changes observed in the test specimens and the actual microstructural variations during hot forming.

3.3 Inverse Analysis FEM

The results of the inverse analysis of the wedge tests, conducted through finite element simulations, are presented below. The critical parameters that influence the mechanical behavior of the material, such as strain, strain rate, and temperature, were examined in detail.

Figure 7 shows the distribution of equivalent strain in the wedge section after compression. The initial geometry was designed to allow for the analysis of a wide range of strains, varying between 0.2 and 2.4. This analysis is crucial, as the degree of strain is directly related to microstructure refinement. Regions subjected to higher strains tend to exhibit finer grains, which in turn leads to an increase in material strength (Ref 29-31).

Strain rate is another crucial parameter that influences recrystallization during the deformation process, directly impacting microstructure refinement. Since recrystallization is a time-dependent process, increasing the strain rate ($\dot{\varphi}$) reduces the time available for the formation of new grains, thus limiting microstructure refinement.

Figure 8 illustrates the variation in strain rate as a function of press displacement at 10 points along the wedge section. Due to the wedge geometry, some regions (P7, P8, P9, and P10) experience deformation throughout the entire process, while others (P1 and P2) undergo deformation only in the final stages of press displacement. This behavior is reflected in the observed strain rate values.

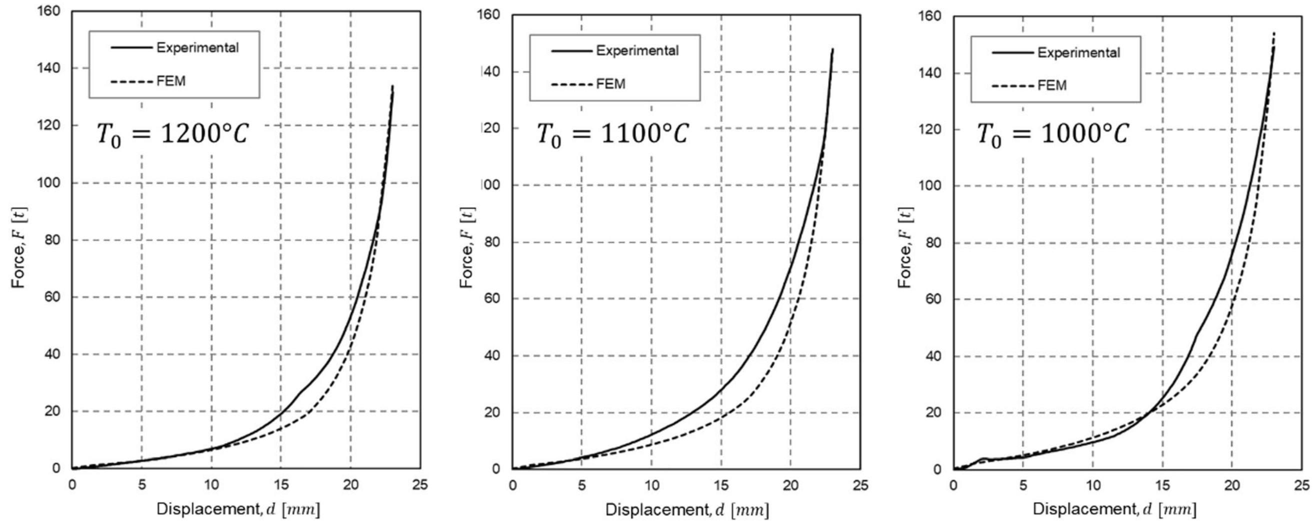

Fig. 6 Evolution of force as a function of press displacement during the forging of the wedges

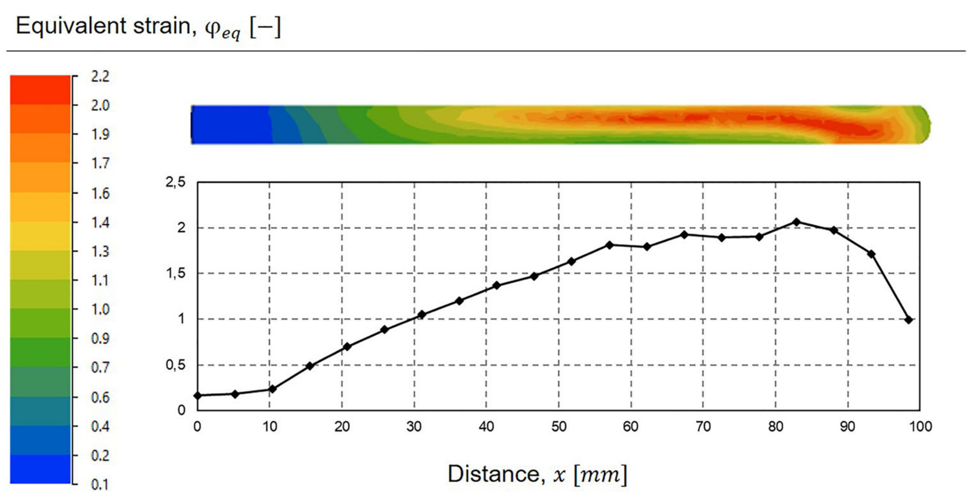

Fig. 7 Distribution of equivalent strain along the wedge section after forging

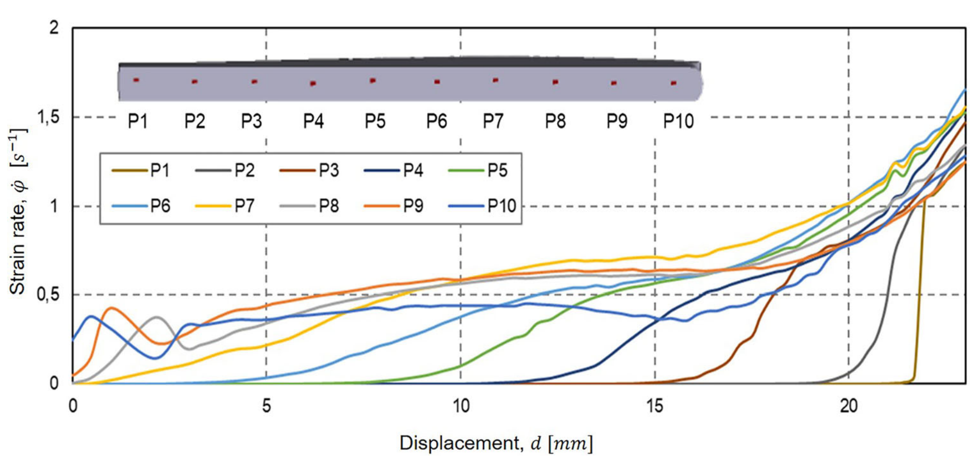

Fig. 8 Variation of strain rate as a function of press displacement at 10 points along the wedge section

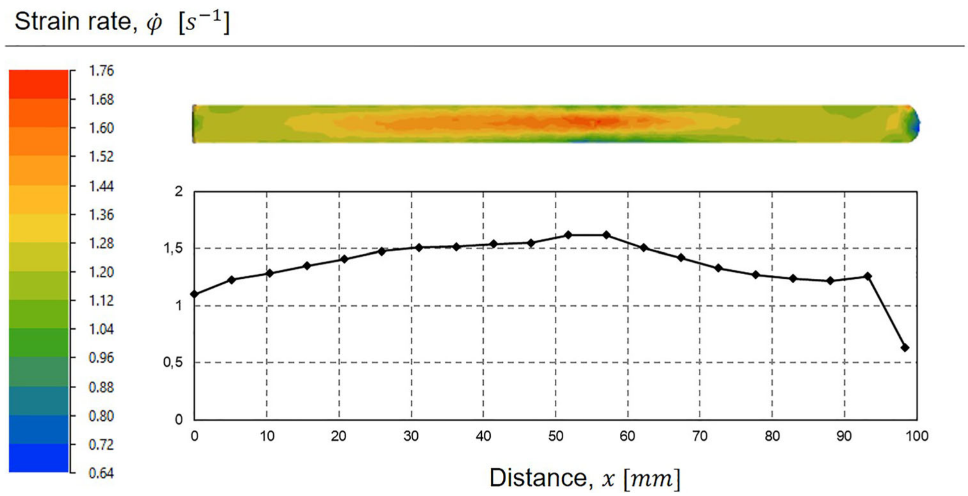

Fig. 9 Distribution of strain rate along the wedge section after forging

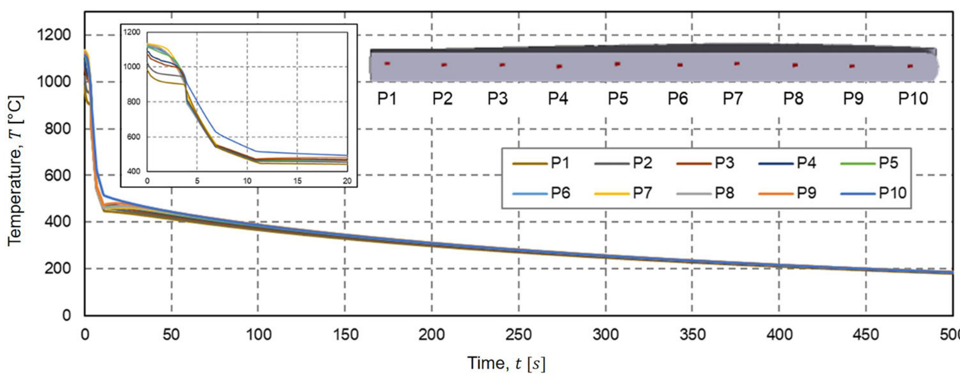

Fig. 10 Variation of temperature as a function of time at 10 points along the wedge section

The distribution of strain rate along the wedge section at the end of the process is shown in Fig. 9. Due to the low speed of the hydraulic press, strain rate values range from 0.4 to 1.7 s^{-1}.

The tests were conducted at three different temperatures, affecting factors such as friction and heat exchange, which could potentially influence material flow during forging. However, the numerical simulations did not reveal significant changes in the deformation profile and strain rate distribution in the wedge section that would justify a more in-depth analysis.

Numerical simulation allows tracking the entire thermal history of the piece during processing. Figure 10 shows the evolution of temperature over time during forging and subsequent continuous cooling at 10 points along the wedge section heated to 1200 °C. Due to thermal losses from radiation and convection during the transfer of the wedge from the furnace to the press, the piece exhibits a thermal gradient from 1130 to 980 °C at the start of forging. As forging begins, a sharp drop in temperature is observed, with the severity varying depending on the region of the piece and the contact time with the tools. The areas that remain in contact with the forging dies for a longer period experience a more pronounced temperature reduction, leading to a decrease in the thermal gradient of the piece. During the initial stage of continuous air cooling, temperature equalization occurs due to heat exchange between the core and the surface of the piece. As a result, the thermal gradient is nearly eliminated, and over time, the cooling curves become almost identical.

Figure 11 shows the temperature distribution in the wedge section after compression, for the three analyzed temperatures. It is observed that the temperature is higher at the end of the piece with a larger volume and gradually decreases toward the opposite end. The lower surface of the piece experiences more intense cooling than the upper surface, as after the press opens, the lower surface remains in contact with the lower die until the piece is extracted.

The cooling profiles observed in the piece heated to 1200 °C (Fig. 9) are repeated in the pieces heated to 1100 °C and 1000 °C, with the same temperature distribution, though with different magnitudes. At the end of forging, the piece heated to 1100 °C shows an average temperature 25 °C lower than the piece initially heated to 1200 °C. Meanwhile, the piece heated to 1000 °C has an average temperature 28 °C lower than the piece heated to 1100 °C.

3.4 Final Microstructure

Three distinct regions of the piece were selected for microstructural analysis: region R_1, which corresponds to the

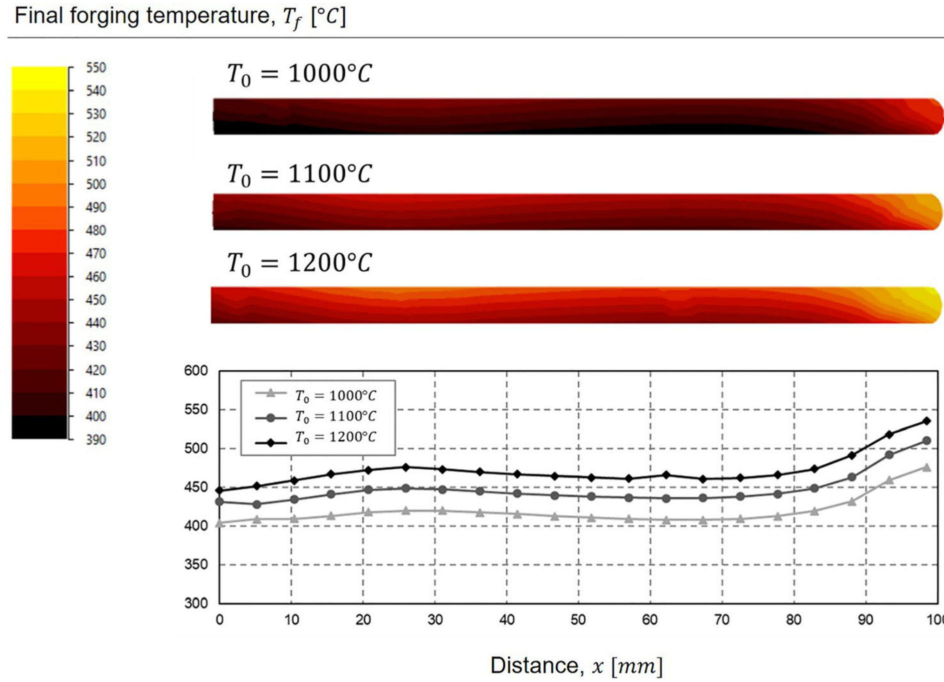

Fig. 11 Temperature distribution along the wedge section after forging

area with the lowest strain ($\varphi_{eq} = 0.5$); region R_2, representing the area with medium strain ($\varphi_{eq} = 1.25$); and region R_3, where the strain is most intense ($\varphi_{eq} = 2$). Figure 12 presents the prior austenitic microstructure of the forged wedges after heating to 1000 °C, 1100 °C, and 1200 °C, respectively.

In the region with the lowest strain, the grains exhibit a polygonal morphology. As the strain severity increases, there is intense refinement of the austenitic structure due to recrystallization. The increase in strain enhances the driving force for dynamic recrystallization, resulting in a substantial increase in the number of small grains. These new grains remain small because the thermodynamic potential generated within them, due to the continuous deformation, prevents further growth. As the thermodynamic potential difference across the new grain boundaries decreases, their growth is halted (Ref 32).

Severely deformed regions at $T_0 = 1000^{\circ}$C and $T_0 = 1100^{\circ}$C also exhibit a few larger grains that have not recrystallized. These grains appear elongated with serrated boundaries. The formation of undulations along the grain boundaries occurs during dynamic recovery. This phenomenon involves short-range migrations of grain boundaries due to the thermodynamic potential generated by dislocations. The boundaries migrate in both directions, acquiring a wavy appearance. In austenite, such undulations indicate the onset of recrystallization (Ref 33). In the wedge forged at $T_0 = 1200^{\circ}$C, recrystallization is more uniform, and larger grains are not observed.

The austenitization of the material (without deformation) at 1000 °C, 1100 °C, and 1200 °C produced austenitic grains with average sizes of 16 μm, 35 μm, and 47 μm, respectively. In the low-deformation region (R_1), the wedges heated to 1100 °C and 1200 °C maintained the original grain size. However, the material forged after heating to 1000 °C showed coarsening of the austenitic structure. The low deformation in this region allows recrystallized grains to continue growing, with growth being interrupted only when the grains meet their neighboring grains also growing, a phenomenon known as impingement.

Figure 13, 14, and 15 shows the final microstructure of the forged wedges after heating to 1000 °C, 1100 °C, and 1200 °C, respectively. The micrographs indicate the predominant formation of bainitic microstructures, with proeutectoid ferrite being avoided under all analyzed conditions. The images reveal the presence of granular bainite and lath bainite (Ref 24, 34-36). With the magnification provided by SEM (scanning electron microscopy), the microconstituents are more clearly identified: bainitic ferrite appears in the darker areas, while carbon-rich microconstituents stand out in the lighter or raised regions. The refinement and complexity of the structures make it challenging to identify the carbon-rich phases. The carbon-rich second phase is a transformation product that can originate from carbon-enriched austenite. It may consist of degenerated pearlite, cementite debris, bainite, mixtures of incomplete transformation products, martensite, retained austenite, or martensite (Ref 37).

Granular bainite is a typical morphology of low-carbon steels subjected to continuous cooling. Although microscopy does not allow for precise identification of the carbon-rich microconstituents, granular bainite is distinguished by the absence of carbides in the microstructure, unlike conventional bainites. During transformation, carbon partitions from bainitic ferrite to the surrounding austenite, enriching and stabilizing the austenite in carbon (Ref 38). As a result, the carbon-rich microconstituent consists of aggregates of retained austenite and martensite, commonly referred to as M/A (martensite/austenite). Granular bainite is usually obtained through contin-

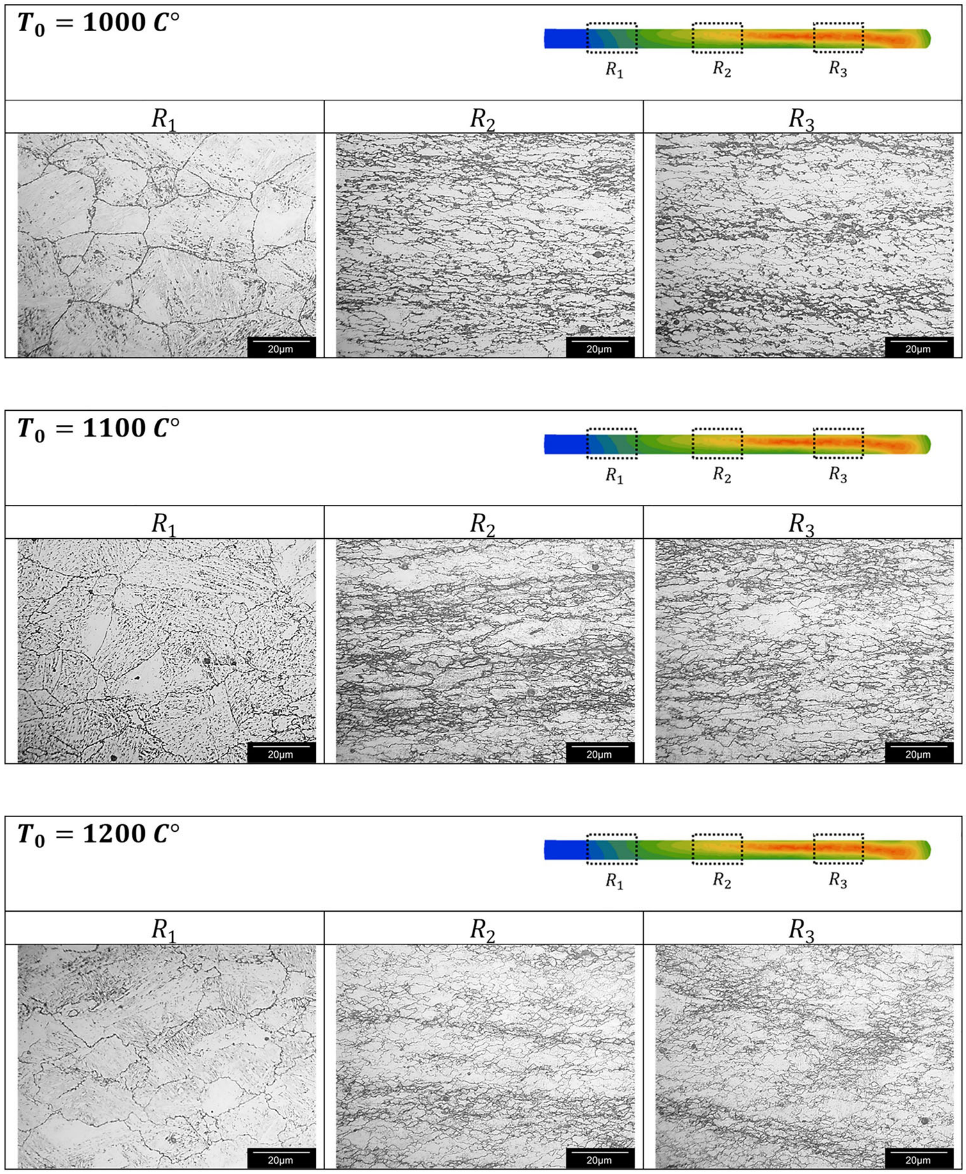

Fig. 12 Prior austenitic structure of the forged wedges (picral etching, 500x magnification)

uous cooling at moderate cooling rates, such as those observed during air cooling (Ref 39, 40).

The impact of deformation on the microstructure is clearly visible in the final micrographs of the wedges. In all analyzed conditions, the less deformed regions (R_1) exhibit a coarser microstructure compared to the more deformed zones (R_2 and R_3). Although the difference in microstructural refinement between zones R_2 and R_3 is subtle, the microstructures in R_3 are generally more refined. Optical micrographs reveal that granular bainite predominates in regions R_2 and R_3. In contrast, the less deformed region displays a microstructure consisting of irregular ferrite grains accompanied by ferrite laths, indicating the formation of upper bainite.

The presence of niobium in the steel plays a crucial role in achieving the refined microstructure observed after forging. Nb significantly delays austenite recrystallization and exerts a solute drag effect on grain boundaries and dislocation movement (Ref 41, 42), thereby contributing to the overall refinement of the microstructure. Even additions in concentrations below 0.04% by weight, as observed in the analyzed steel, are sufficient to have a significant effect on the microstructure (Ref 43).

3.5 Hardness

Figure 16 shows the hardness profile of the forged wedges after heating to 1000, 1100, and 1200 °C. In all conditions,

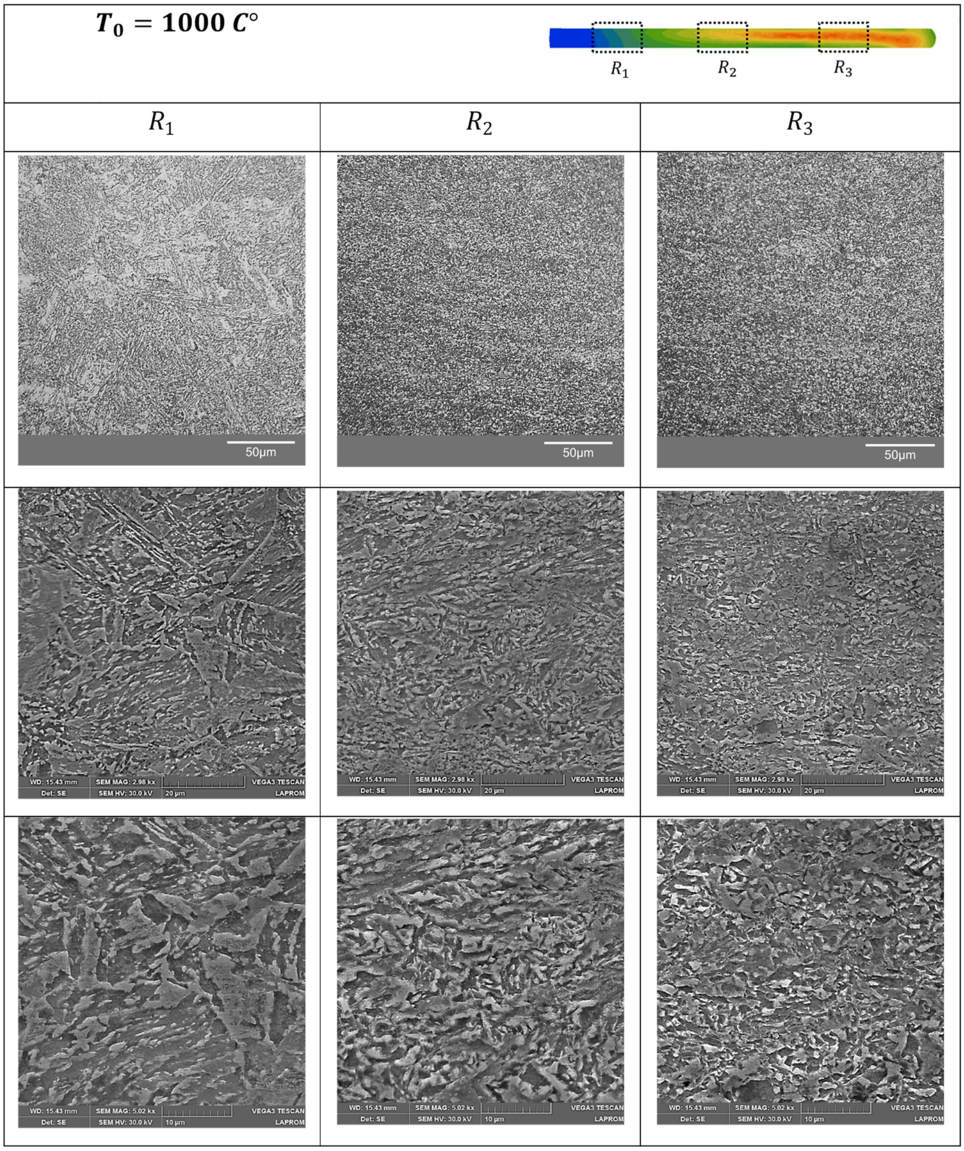

Fig. 13 Micrographs of the forged wedge after heating to 1000 °C (2% nital etching, magnifications of 500x, 3000x, and 5000x)

there is a trend of increasing hardness along the wedge, from the region with less deformation to the region with more deformation. The hardness increase is moderate at 1000 and 1100 °C, but it becomes more pronounced in the wedge forged at 1200 °C. At 1000 °C, the region with the least deformation exhibits hardness between 240 and 300 HV, while in the region with the most deformation, the hardness reaches around 350 HV. Overall, forging at 1100 °C resulted in a higher hardness compared to the piece heated to 1000 °C, with maximum values ranging between 375 and 390 HV. The piece forged at 1200 °C showed more consistent results, with less fluctuation and a gradual increase in hardness. In this condition, hardness values exceeding 400 HV were observed, with a maximum value reaching 472 HV.

These results are consistent with previous studies. Silveira et al. (Ref 9) observed a similar hardness trend in bainitic steel DIN 18MnCrSiMo6-4 forged under the same conditions. The authors noted that the reduction in heating and forging temperature leads to a higher volumetric fraction of polygonal ferrite, which lowers the steel's hardness to values close to 300 HV. Cao et al. (Ref 44) demonstrated that, for the same cooling rate, an increase in forging temperature enhances the strength of

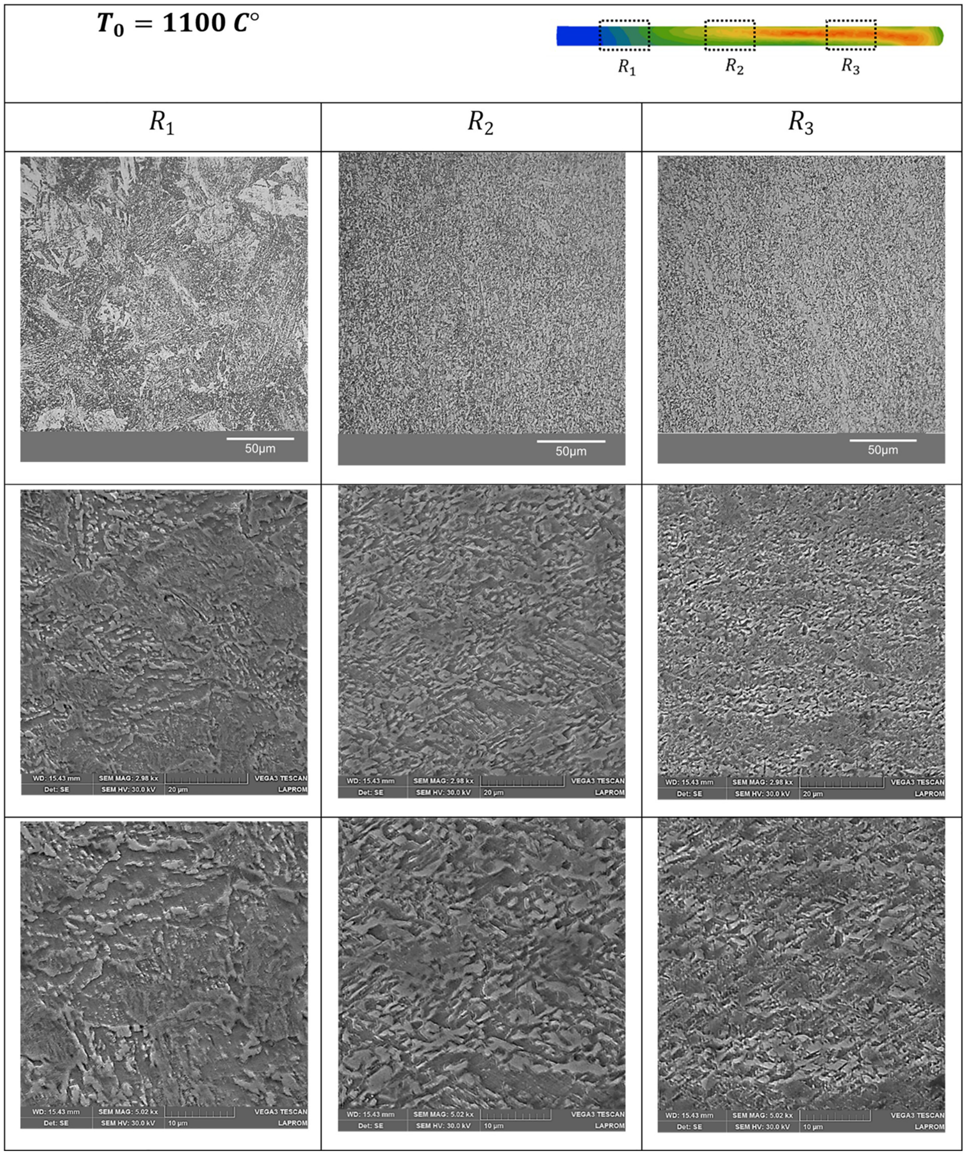

Fig. 14 Micrographs of the forged wedge after heating to 1100 °C (2% nital etching, magnifications of 500x, 3000x, and 5000x)

the bainitic microstructure. According to the authors, this effect occurs due to the greater formation of lath bainite, rather than granular bainite.

4. Summary of Results

Figure 17 summarizes the variation in hardness of the forged wedges as a function of deformation, strain rate, and cooling rate. During continuous cooling, the temperature of the pieces remains relatively homogeneous, resulting in minimal variation in the cooling rate. Thus, the cooling rate considered corresponds to the thermal loss from the time the piece leaves the furnace until the start of continuous cooling.

The graphs highlight the influence of strain rate on the final hardness of the material. During processing at 1200 °C, hardness increases as the strain rate rises, stabilizing at a plateau at higher levels of deformation. This indicates that under these conditions, a higher strain rate tends to result in higher hardness values, especially at intermediate levels of deformation. For forging at 1000 °C and 1100 °C, hardness also benefits from a higher strain rate, though it is less sensitive to small variations in parameters.

The graphs also suggest that controlling the cooling rate is crucial for optimizing hardness, particularly at higher temper-

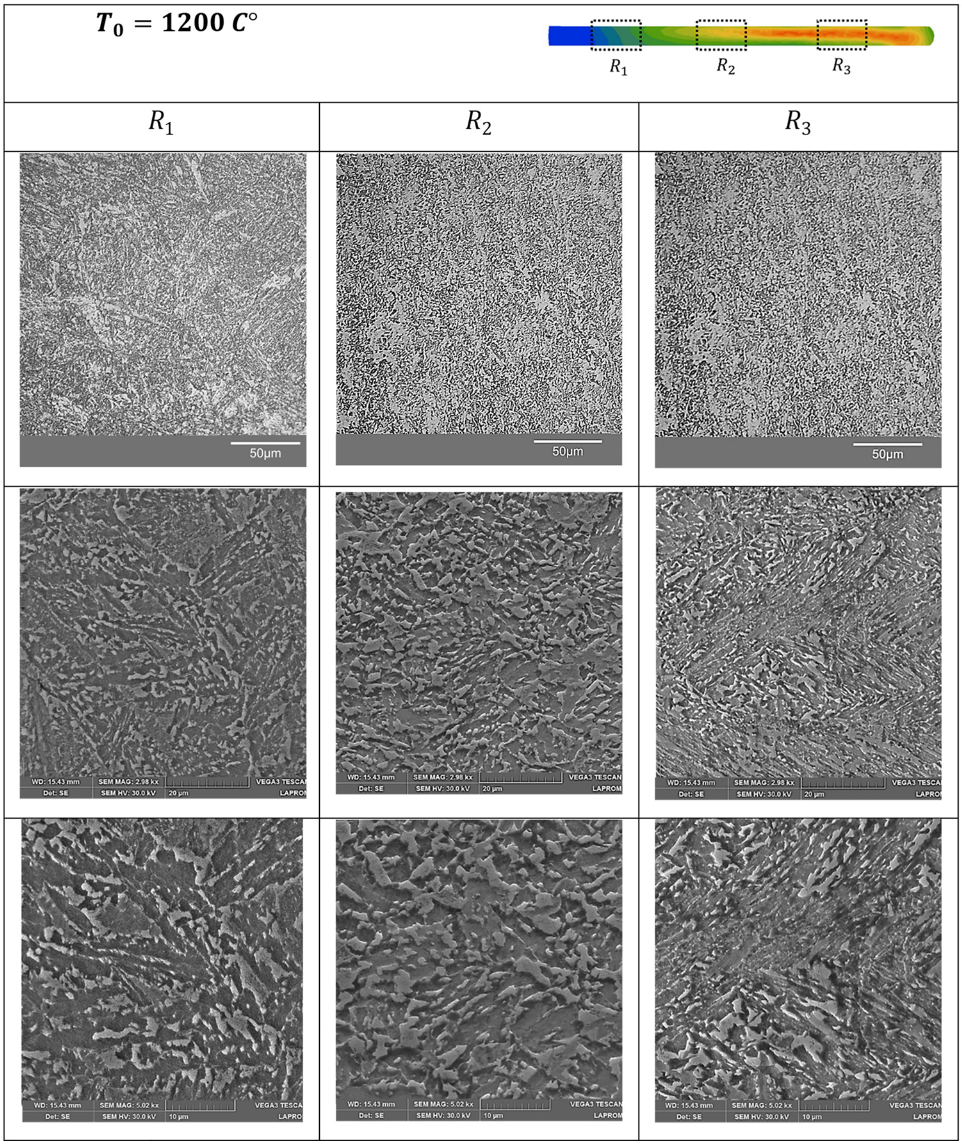

Fig. 15 Micrographs of the forged wedge after heating to 1200 °C (2% nital etching, magnifications of 500x, 3000x, and 5000x)

atures and deformations. A more severe cooling increases the hardness of bainite, as the bainitic transformation occurs at lower temperatures. The reduction in transformation temperature refines the microstructure, resulting in increased material strength (Ref 45).

The evaluation of the austenitization parameters demonstrated that in the absence of plastic deformation, heating to 1200 °C significantly thickens the austenitic microstructure compared to treatments at 1000 °C and 1100 °C (Fig. 3). However, as shown in Fig. 12, when the material is subjected to plastic deformation, the behavior changes. The increase in temperature promotes dynamic recrystallization, so that after thermomechanical processing, the structure obtained at $T_0 = 1200^\circ\mathrm{C}$ becomes as refined or even more refined than the structures resulting from treatments at $T_0 = 1000^\circ\mathrm{C}$ and $T_0 = 1100^\circ\mathrm{C}$. This effect is even more pronounced in regions that experienced higher deformations.

During hot forming, temperature, in combination with strain and strain rate, directly influences recrystallization (Ref 46, 47). The final microstructures of the wedges indicate that the combination of these parameters did not compromise the homogeneity of the recrystallized microstructure, even in regions subjected to severe deformation. This suggests that the deformation of bainitic steels in low-speed presses is beneficial. In high-speed equipment, the combination of severe deformation with high strain rates may result in incomplete recrystallization of the material, compromising the mechanical properties of the bainitic forging (Ref 48). As the strain rate

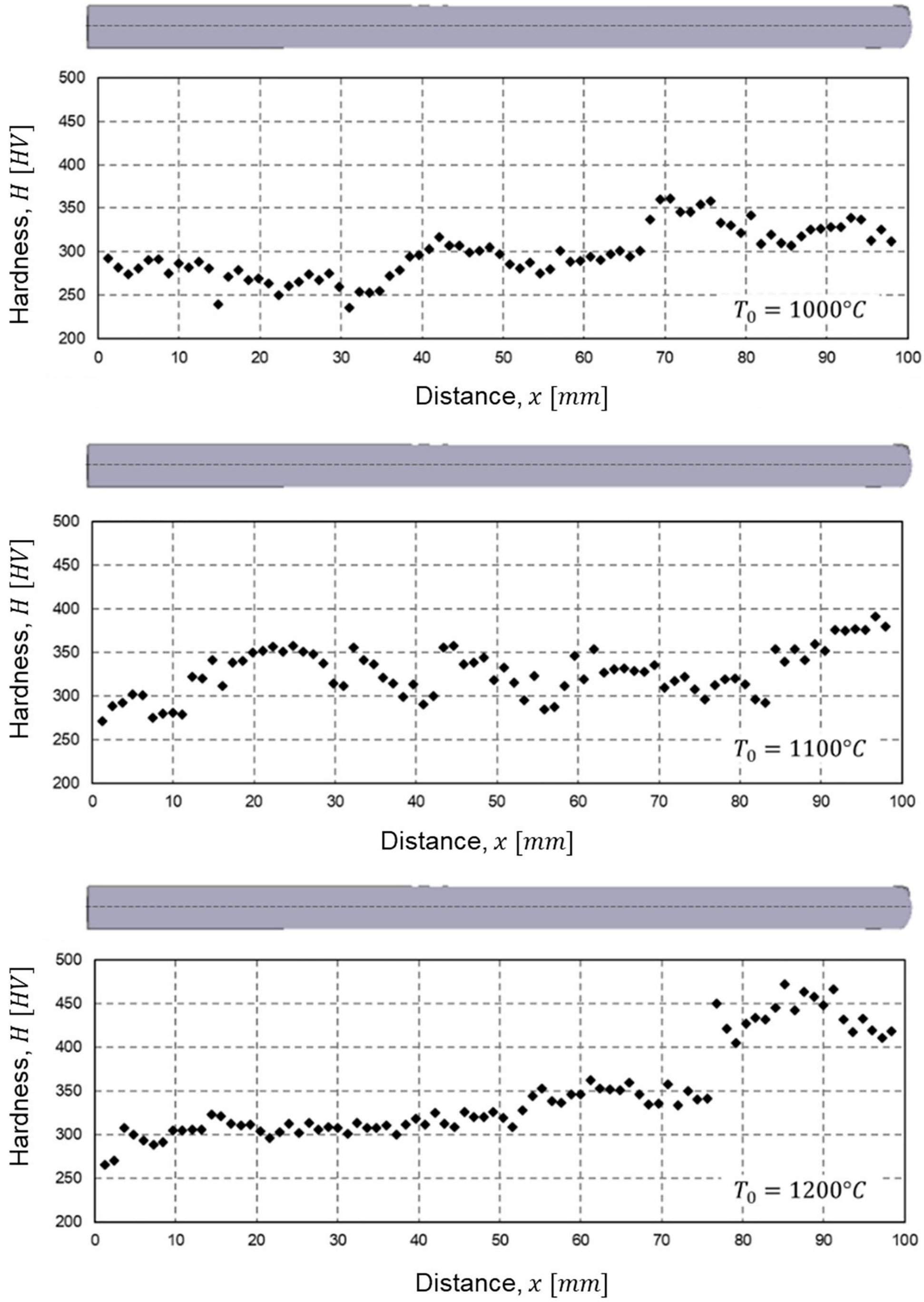

Fig. 16 Hardness profiles of the forged wedges

increases, grain growth appears to be limited. This occurs because the reduced formation time restricts the growth of dynamically recrystallized grains under high strain rates (Ref 49).

5. Conclusions

The forgeability analysis of the microalloyed steel with the composition 0.18C-1.38Mn-0.36Si-0.47Cr-0.03Mo-0.05Al-0.04Nb-0.01Ti revealed the following results:

- The wedge tests revealed that hot forging followed by continuous air cooling results in homogeneous microstructures, predominantly composed of granular bainite, with the presence of lath bainite.
- Although the microstructure remains uniform under all tested conditions, hardness profiles indicate that thermomechanical parameters significantly affect the hardness of the forged material.
- The steel demonstrated strong potential for applications in hot forging followed by continuous cooling, offering an economically and energetically efficient solution, eliminating the need for additional heat treatments.

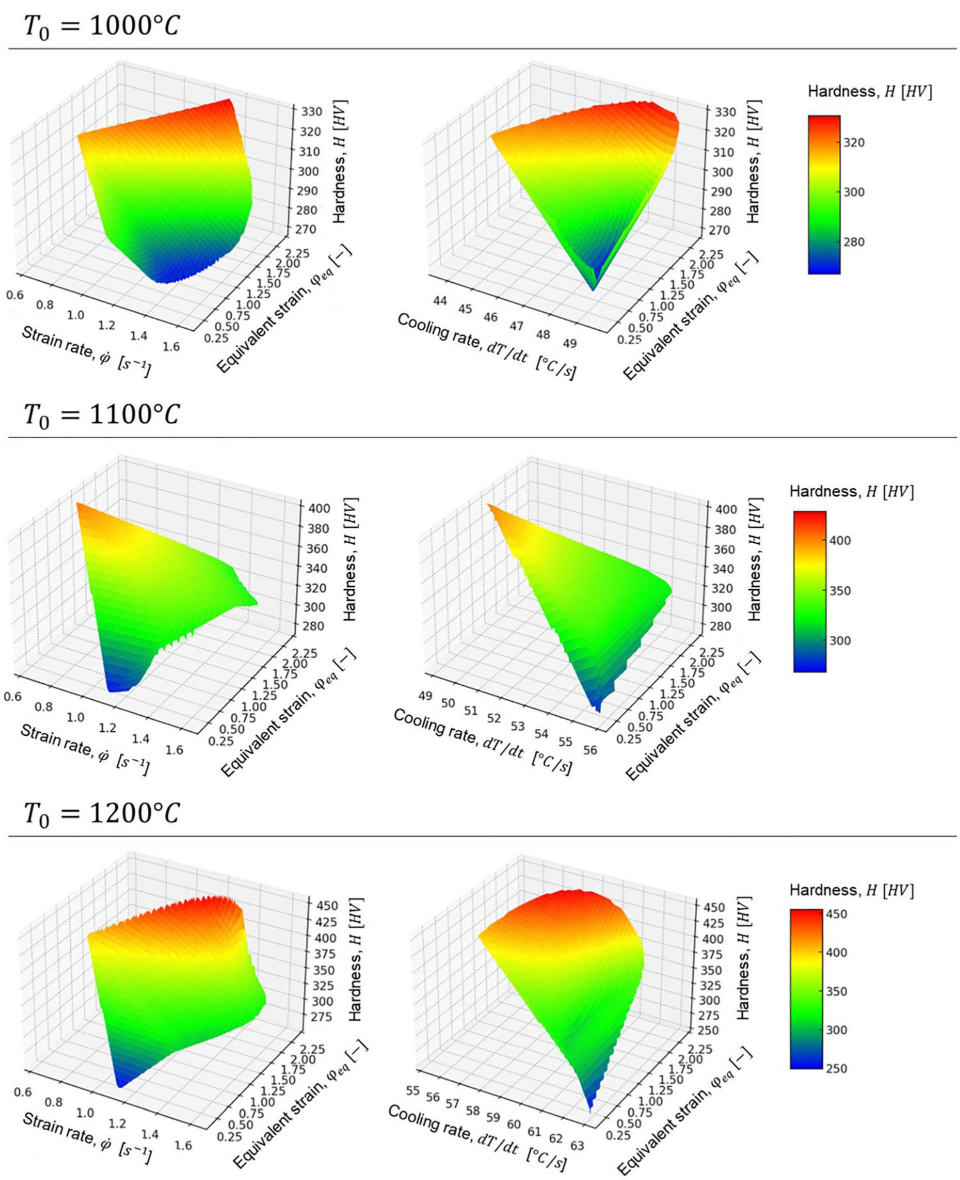

Fig. 17 Variation in hardness of the forged wedges as a function of deformation, strain rate, and cooling rate

- Due to the dimensions of the wedge test samples, the results are more applicable to small-volume or thin-walled components. For larger components, which experience different cooling conditions, further investigation under similar conditions is required.

Acknowledgments

The authors thank CNPq, CAPES and FAPERGS for financial support (FAPERGS/CAPES 06/2018, process: 19/2551-0000710-8);(CNPq/MCTI/FNDCT nº 18/2021, process: 404196/2021-7);(CNPq research productivity—PQ1-4/2021; PDJ—25/2021 150252/2022-6; GD—2019); (CNPq process: 309188/2021-0); (CNPq process: 446930/2023-7); (CNPq process:408298/2023-5); (CAPES (PROEXIES-2020); and the Metalforming Laboratory (LdTM) and Mineral Processing Laboratory (LAPROM). for technical support.

Conflict of interest

The authors certify that they have no affiliations with or involvement in any organization or entity with any financial interest, or non-financial interest in the subject matter or materials discussed in this manuscript.

Ethical Approval

Not applicable.

References

1. Fortune Business Insights. Metal forging market size, share & industry analysis, by raw material (carbon steel, alloy steel, stainless steel, aluminum, magnesium, titanium, and others), by technology (closed die, open die, and others), by end-user (automotive, mechanical equipment, aerospace & railways, and others), and regional forecast, pp 2024–2032. (2024), Disponível em: https://www.fortunebusinessinsights.com/metal-forging-market-103175
2. W. Hagedorn, A. Gramlich, K. Greiff, and U. Krupp, Alloy and Process Design of Forging Steels for Better Environmental Performance, *Sustain. Mater. Technol.*, 2022, **34**, p e00509
3. G.-W. Raedt, U. Speckenheuer, and K. Vollrath, New Forged Steels Energy-efficient Solutions for Stronger Parts, *Cover Story Mater.*, 2012, **12**, p 12–17
4. C. Kremer and K. Muller-Babic, Connecting Rods Made of Micro-alloyed Forged Steel, *MTZ Worldw.*, 2020, **81**, p 52–55
5. Bleck W, Moeller E, and Bleck W (Ed.) (2017) Handbuch Stahl. Auswahl, Verarbeitung, Anwendung. Hanser Verlag, München. ISBN: 978-3-446-44961-9
6. K.-I. Sugimoto, T. Hojo, and A.K. Srivastava, Low and Medium Carbon Advanced High-Strength Forging Steels for Automotive Applications, *Metals*, 2019, **9**, p 1263. https://doi.org/10.3390/met9121263
7. C. Keul, V. Wirths, and W. Bleck, New Bainitic Steels for Forgings, *Arch. Civ. Mech. Eng.*, 2012, **12**(2), p 119–125
8. W. Hui, Y. Zhang, X. Zhao, N. Xiao, and F. Hu, High Cycle Fatigue Behavior of V-Microalloyed Medium Carbon Steels: A Comparison Between Bainitic and Ferritic-Pearlitic Microstructures, *Int. J. Fatigue*, 2016, **91**, p 232–241
9. A.C.F. Silveira, W.L. Bevilaqua, V.W. Dias, P.J. de Castro, J. Epp, and A.S. Rocha, Influence of Hot Forging Parameters on a Low Carbon Continuous Cooling Bainitic Steel Microstructure, *Metals*, 2020, **10**, p 601. https://doi.org/10.3390/met10050601
10. W. Wirths, R. Wagener, W. Bleck, and T. Melz, Bainitic Forging Steels for Cyclic Loading, *Adv. Mat. Res.*, 2014, **922**, p 813–818
11. A. Gramlich, R. Lange, U. Zitz, and K. Büßenschütt, Air-Hardening Die-Forged Con-Rods—Achievable Mechanical Properties of Bainitic and Martensitic Concepts, *Metals.*, 2022, **12**, p 97
12. E. Erisir, I.I. Ayhan, C. Guney, E. Alan, N.B. Dürger, and U. Sibel, Microstructure and Phase Transformations in High-Strength Bainitic Forging Steel, *JMEPEG*, 2021, **30**, p 3458–3467. https://doi.org/10.1007/s11665-021-05689-1
13. Stieben A, Bleck W, and Schönborn S (2016) Lufthärtender duktiler stahl mit mittlerem mangangehalt für die massivumformung. *MassivUmformung*
14. A. Gramlich, T. Schmiedl, S. Schönborn, T. Melz, and W. Bleck, Development of Air-Hardening Martensitic Forging Steels, *Mater. Sci. Eng. A*, 2020, **784**, p 139321
15. A. Gramlich, C. van der Linde, M. Ackermann, and W. Bleck, Effect of molybdenum, aluminium and boron on the phase transformation in 4 wt.–% manganese steels, *Results Mater.*, 2020, **8**, p 100147
16. G.E. Dieter, H.A. Kuhn, and S.L. Semiatin, *Handbook of Workability and Process Design*, ASM International, West Conshohocken, 2003
17. G.E. Dieter, Workability Testing Technique. *ASM* (1984)
18. J.J. Park and S. Kobayashi, Three-Dimensional Finite-Element Analysis of Block Compression, *Int. J. Mech. Sci.*, 1984, **26**, p 165
19. V.K. Jain, L.E. Matson, H.L. Gegel, and R. Srinivasan, Physical modeling of metalworking processes ii: comparison of viscoplastic modeling and computer simulation, *Physical Modeling of Metalworking Processes*. E. Erman, S.L. Semiatin Ed., TMS, Warrendale, 1987, p 127
20. M.H. Parsa, M.N. Ahmadabadi, H. Shirazi, B. Poorganji, and P. Pournia, Evaluation of Microstructure Change and Hot Workability of High Nickel High Strength Steel Using Wedge Test, *J. Mater. Process. Technol.*, 2008, **199**, p 304–313
21. ASTM International, *Standard Test Methods for Determining Average Grain Size*, ASTM International, West Conshohocken, 2014, p 1–28
22. R.C. Chen, C. Hong, J.J. Li, Z.Z. Zheng, and P.C. Li, Austenite Grain Growth and Grain Size Distribution in Isothermal Heat-Treatment of 300M Steel, *Procedia Eng.*, 2017, **207**, p 663–668
23. G.W. Yang, X.J. Sun, Q.L. Yong, Z.D. Li, and X.X. Li, Austenite Grain Refinement and Isothermal Growth Behavior in a Low Carbon Vanadium Microalloyed Steel, *J. Iron. Steel Res. Int.*, 2014, **21**(8), p 757–764
24. J. Fernández, S. Illescas, and J.M. Guilemany, Effect of Microalloying Elements on the Austenitic Grain Growth in a Low Carbon HSLA Steel, *Mater. Lett.*, 2007, **61**, p 2389–2392
25. L.Y. Lan, C.L. Qiu, D.W. Zhao, X.H. Gao, and L.X. Du, Effect of Austenite Grain Size on Isothermal Bainite Transformation in Low Carbon Microalloyed Steel, *Mater. Sci. Technol.*, 2011, **27**, p 1657–1663
26. A. Chamanfar, S.M. Chentouf, M. Jahazi, and L.P. Lapierre-Boire, Austenite Grain Growth and Hot Deformation Behavior in a Medium Carbon Low Alloy Steel, *J. Market. Res.*, 2020, **9**(6), p 12102–12114
27. J. Krawczyk and H. Adrian, The Kinetics of Austenite Grain Growth in Steel for Wind Power Plant Shafts, *Arch. Metall. Mater.*, 2010, **55**(1), p 91–99
28. N. Tsuji, Y. Saito, H. Utsunomiya, and S. Tanigawa, Ultra-Fine Grained Bulk Steel Produces by Accumulative Roll-Bonding (arb) Process, *ScriptaMateriali*, 1999, **40**(7), p 795–800
29. B. Baudelet, J. Languillaume, and G. Kapelski, Microstructure and Mechanical Properties of Ultrafine-Grained Materials, *Key Eng. Mater.*, 1994, **97–98**, p 125–140
30. A. Lasalmonie and J.L. Strudel, Influence of Grain Size on the Mechanical Behaviour of Some High Strength Materials, *J. Mater. Sci.*, 1986, **21**, p 1837–1852
31. J. Humphreys, G.S. Rohrer, and A. Rollett, *Recrystallization and Related Annealing Phenomena*, 3rd ed. Elsevier, Amsterdam, 2017
32. H. McQueen, Formation and Application of Grain Boundary Serrations, *Can. Metall. Q.*, 1995, **34**(3), p 219–229
33. R.A. Hatwig, J. Dong, J. Epp, and A.S. Rocha, Effect of Compressive Deformations on the Final Microstructure of a Low Carbon High Silicon Bainitic Steel Thermomechanically Processed, *Mat. Res.*, 2021, **24**(1), p e20200346
34. J.S. Kang, J.B. Seol, and C.G. Park, Three-Dimensional Characterization of Bainitic Microstructures in Low-Carbon High-Strength Low-Alloy Steel Studied by Electron Backscatter Diffraction, *Mater Charact*, 2013, **79**, p 110–121
35. J. Kang et al., Improvement of strength and toughness for hot rolled low-carbon bainitic steel via grain refinement and crystallographic texture, *Mater. Lett.*, 2016, **175**, p 157–160
36. M. Müller, D. Britz, L. Ulrich, T. Staudt, and F. Mücklich, Classification of Bainitic Structures Using Textural Parameters and Machine Learning Techniques, *Metals*, 2020, **10**, p 630. https://doi.org/10.3390/met10050630
37. H.K.D.H. Bhadeshia, *Bainite in Steels*, 2nd ed. Institute of Materials, Maney Publishin, London, 2001
38. L. Morales-Rivas, Viewpoints on Technological Aspects of Advanced High-Strength Bainitic Steels, *Metals*, 2022, **12**, p 195. https://doi.org/10.3390/met12020195
39. H. Fang et al., Creation of Air-Cooled Mn Series Bainitic Steels, *J. Iron. Steel Res. Int.*, 2008, **15**(6), p 1–9
40. C. Feng et al., Mn-Series Low-Carbon Air-Cooled Bainitic Steel Containing Niobium of 0.02%, *J. Iron. Steel Res. Int.*, 2010, **17**(4), p 53–58
41. Hasler S, et al. (2011) New air cooled steels with outstanding impact toughness. In: *3rd International Conference on Steels in Cars and Trucks*, Salzburg
42. G.K. Bansal, V.C. Srivastava, and S. Ghosh Chowdhury, Role of Solute Nb in Altering Phase Transformations during Continuous Cooling of a Low-Carbon Steel, *Mater. Sci. Eng. A*, 2019, **767**, p 138416
43. X. Chen, F. Wang, C. Li, and J. Zhang, Dynamic Continuous Cooling Transformation, Microstructure and Mechanical Properties of Medium-Carbon Carbide-Free Bainitic Steel, *High Temp. Mater. Process.*, 2020, **39**, p 304–316
44. J. Cao et al., Effects of Thermomechanical Processing on Microstructure and Properties of Bainitic Work Hardening Steel, *Mater. Sci. Eng. A*, 2015, **639**, p 192–197
45. B. Buchmayr, Critical Assessment 22: Bainitic Forging Steels, *Mater. Sci. Technol.*, 2016, **32**, p 517–522
46. Y.C. Lin, X.Y. Wu, X.M. Chen, J. Chen, D.X. Wen, J.L. Zhang, and L.T. Li, EBSD Study of a Hot Deformed Nickel-Based Superalloy, *J. Alloys Compd.*, 2015, **640**, p 101–113
47. D.G. He, Y.C. Lin, J. Chen, D.D. Chen, J. Huang, Y. Tang, and M.S. Chen, Microstructural Evolution and Support Vector Regression Model

for an Aged Ni-Based Superalloy During Two-Stage Hot Forming with Stepped Strain Rates, *Mater. Design*, 2018, **154**, p 51–62

48. Z. Yang, F. Zhang, C. Zheng, M. Zhang, B. Lv, and L. Qu, Study on Hot Deformation Behaviour and Processing Maps of Low Carbon Bainitic Steel, *Mater. Des.*, 2015, **66**, p 258–266
49. X.M. Chen, Y.C. Lin, D.X. Wen, J.L. Zhang, and M. He, Dynamic Recrystallization Behavior of a Typical Nickel-Based Superalloy during Hot Deformation, *Mater. Design*, 2014, **57**, p 568–577